AIAA 2007-944

45th AIAA Aerospace Sciences Meeting and Exhibit Conference
Jan. 8- 11, 2007, Reno, Nevada

AIAA 2007-0944

Numerical Simulation of Surface Roughness Effects on Receptivity of Hypersonic Flow over Blunt Cones

Xiaolin Zhong[1]
University of California, Los Angeles, California 90095

Abstract

A numerical simulation study has been conducted on the receptivity of Mach 7.99 hypersonic flow over a blunt cone with imbedded azimuthal arrays of isolated surface roughness on the cone surface. Surface roughness has been shown to have profound effects on boundary layer transition. Recent research has shown that one possible explanation to bypass transition is the transient growth theory. However, there has not been any direct numerical simulation study on transient growth in hypersonic boundary layers. Furthermore, it is not known how the optimal disturbances computed by the transient growth theory are generated by surface roughness. This paper presents some initial results in our on-going numerical simulation study on the receptivity of the hypersonic boundary layers to stationary surface roughness without any freestream forcing waves. The flow conditions are those of Stetson's 1984 wind-tunnel experiments for Mach 7.99 flow over a 7° half-angle blunt cone. The simulation results show that the roughness element generates streamwise vortices inside the boundary layer. In the computational domain studied in this paper, the induced perturbation mainly decays after the roughness. No strong transient growth appears immediately behind the roughness element. Further studies are needed to study the effects of longer computational domains and the effects of other isolated and distributed roughness elements.

1 Introduction

The accurate prediction of laminar-turbulent transition in hypersonic boundary layers is a critical part of the aerodynamic heating analyses on hypersonic vehicles. Despite decades of extensive research, the prediction of hypersonic boundary-layer transition is still mostly based on empirical correlation methods or the semi-empirical e^n method because a number of physical mechanisms leading to transition are currently not well understood. The receptivity phenomenon, which is the process of environmental disturbances initially entering the boundary layers and generating disturbance waves, is one of these important, but less understood, mechanisms.

Stetson *et al.*[1, 2] carried out boundary-layer stability experiments on an axisymmetric blunt cone in a Mach 7.99 freestream. The half angle of the cone was 7°, the nose radii were 1.5 inches and larger, and the freestream Reynolds number based on the nose radius was 33,449. The Reynolds number based on the total length of the cone was about 9 millions. Detailed fluctuation spectra of the disturbance waves developing along the body surface were measured in the experiments. It was found that the disturbances in the boundary layer were dominated by the second mode instability. Significant super harmonic components of the second modes were observed after the second mode

[1]Professor, Mechanical and Aerospace Engineering Department, Associate Fellow, AIAA.

became dominant. Compared with similar hypersonic flow over a sharp cone, the second mode instability of the blunt cone appeared in much further downstream locations. This indicates a stabilization of the boundary layer by slight nose bluntness. Stability experiments of hypersonic flows over sharp or blunt cones have also been carried out by other researchers. Demetriades[3, 4] did extensive stability experiments on hypersonic boundary layers over axisymmetric cones. Recently, Maslov and his colleagues[5, 6] reported their stability experiments on supersonic and hypersonic flows over sharp or blunt cones.

The normal-mode linear stability characteristics of the boundary-layer flow over the same blunt cone as Stetson *et al.*'s experiments have been studied by a number of researchers[7-10]. Malik *et al.* [7] computed the neutral stability curve and compared the growth rates obtained by LST with the experimental results. The steady base flow solution was computed by using the parabolized Navier-Stokes equations. They found that the nose bluntness stabilizes the boundary layer. The growth rates predicted by the LST were compared with Stetson *et al.*'s experimental results at the surface location of $s = 175$ nose radii (0.667 m). The linear stability analyses predicted slightly lower frequency for the dominant second mode, but much higher amplification rates than the experimental results. Rosenboom et al.[11] did further study on the effect of nose bluntness on the linear stability of hypersonic flow over Stetson's blunt cone. In their studies, the cone geometry and freestream conditions were adapted to the Stetson's experiments. Three cases of blunt cones of different nose radii, which cover both ``small" and ``large'' bluntness, were considered. The purpose was to investigate, by linear stability analysis, the transition reversal phenomenon observed in experiments at ``large" bluntness[12, 13]. The transition reversal phenomenon refers to the experimental observation that the transition location moves downstream when the nose radius is increased. This trend is, however, reversed when the nose radius is larger than a certain critical value. Increasing nose radius after that will lead to a forward movement of the transition location. The downstream movement of the transition location at small radii can be explained by the reduction of local Reynolds numbers owing to the entropy layer created by the nose bluntness. However, there is still no satisfactory explanation for the cause of transition reversal at large nose bluntness. By a linear stability analysis, Rosenboom et al. confirmed a monotonic downstream movement of the second mode critical Reynolds number as nose radius increases. However, their linear stability analysis still cannot explain the transition reversal phenomena observed in experiments at ``large" bluntness. Their results indicated that there is a need for better understanding of boundary layer receptivity as well as nonlinear transition phenomena for engineering transition prediction. Because linear stability analysis and recent transient growth theory do not include the receptivity to the surface roughness, direct numerical simulation can fill the gap in such studies.

Zhong et al.[14-16] have conducted numerical simulation of the stability and receptivity of Stetson's Mach 8 flow over blunt cones. In [15], the numerical results for the steady base flow were compared with the experimental results of Stetson et al.[1], and with the numerical results of Esfahanian[17]. In addition, a normal-mode linear stability analysis was used to identify the main components of boundary-layer disturbances generated by forcing freestream fast acoustic waves. It was found that neither the first mode nor the second mode instability waves are excited directly by freestream fast acoustic waves in the early region along the cone surface, although the Mack modes can be unstable there. Instead, the second mode is excited downstream of the second-mode Branch I neutral stability point. The delay of the second-mode excitation is a result of the fact that the hypersonic boundary-layer receptivity is governed by a two-step resonant interaction process: 1) resonant interactions between the forcing waves and a stable boundary-layer wave mode I near the leading edge region, and 2) resonant interactions between the induced stable mode I and the unstable second Mack mode downstream. In [16], we presented a numerical study on the effects of nose bluntness on the receptivity to freestream acoustic waves for hypersonic flow by comparing the results of three nose radii. The flow conditions duplicate the experiments of Stetson et al.[1] and aim to investigate the effects of nose bluntness on receptivity. By using the numerical simulation, the initial receptivity process can be computed accurately in the current study. The effects of bow shock interaction with forcing waves, the effects of the entropy layer and non-parallel boundary layer are also taken into account in the numerical simulation. It was found that the basic receptivity mechanism of hypersonic flow over the blunt cone with different nose radii is essentially the same. As the nose radius increases from ``small" to ``large", the results showed no reversal in the location of instability wave induced by the receptivity process. The location of initial excitation of the second instability mode always moves downstream as the nose bluntness is increased.

The e^n method, which is based on the modal instability, cannot explain bypass transition such as roughness-induced nose-tip transition in hypersonic boundary layers. Recent theoretical studies have shown the importance of transient growth and surface roughness in bypass transition[18-20]. Transient growth is a result of the coupling

between oblique Orr-Sommerfeld and Squire modes, which lead to algebraic growth followed by exponential decay in the early region in the boundary layers. Reshotko and Tumin[21] developed a spatial theory of optimal disturbances in boundary layers. It was found that the most significant transient growth is associated with stationary streamwise vortices.

Surface roughness has been shown to have profound effects on boundary layer transition. Although extensive experiments have been conducted on roughness-induced transition, its mechanisms have not been understood. Reshotko and Tumin[20] proposed a transient-growth model for early transition due to distributed roughness by using computational results based on their spatial transient growth theory. Their transient growth based transition relations reproduce the trend of Reda and the passive nosetip technology (PANT) data[22]. The transient growth theory does not explain the receptivity of the optimal growth associated with stationary streamwise vortices. Instead, Reshotko and Tumin[20] assumed a linear wave growth with respect to the roughness height. The exact receptivity mechanisms of hypersonic boundary layers, which are critical to the explanation of transition by the transient growth theory, are still not known. Recently, White et al.[23, 24] have done a series of experiments on transient growth of stationary disturbances in a flat plate incompressible boundary layer. Direct numerical simulations of White's experiments have been carried out by Choudhari and Fischer[25, 26]. Theoretical analyses have been carried by Tumin and Reshotko[27, 28]. Experimental results indicate that disturbances generated by surface roughness undergo suboptimal growth, which is significantly different from theoretical optimal growth. For hypersonic boundary layers, so far, there has not been any reported computational (or experimental) study on transient growth theory, its receptivity to surface roughness, and its nonlinear breakdown. Such computational simulations can be valuable to the development of a transient-growth model for bypass transition.

Recent research has shown that one possible explanation to bypass transition is the transient growth theory. However, there has not been any direct numerical simulation study on transient growth in hypersonic boundary layers. Furthermore, it is not known how the optimal disturbances computed by the transient growth theory are generated by surface roughness. It is also not clear what the role of freestream disturbances are in the transient growth theory. These are important issues related to the receptivity of transient growth, which need to be resolved. In order to understand the cause of the transition reversal phenomenon and to study the possible role of transient growth hypersonic boundary instability, this paper presents some initial results in our numerical simulation study on the receptivity of the hypersonic boundary layers to stationary surface roughness without any freestream forcing waves. The overall research objective is to conduct extensive direct numerical simulation studies on the early stage of hypersonic boundary layer receptivity related to transient growth of streamwise vortices for hypersonic flow over blunt cones and flat plates. In this paper, we will focus on Stetson's flow conditions of Mach 7.99 flow over a blunt cone. Only results of a single case with nose radius of $r_n = 0.0889m$ are presented in this paper. Numerical simulation studies for other nose radii and various forms of roughness elements are currently under way and will be reported in future papers.

2 Governing Equations and Numerical Methods

The governing equations for both steady and unsteady flow computations are briefly presented in this section. Details of the governing equations and numerical methods for two and three-dimensional flows have been described in previous papers[29-31]. The governing equations are the unsteady three-dimensional Navier-Stokes equations written in the following conservation-law form:

$$\frac{\partial U^*}{\partial t^*} + \frac{\partial F_j^*}{\partial x_j^*} + \frac{\partial F_{vj}^*}{\partial x_j^*} = 0 \tag{1}$$

where $U^* = (\rho^*, \rho^* u_1^*, \rho^* u_2^*, \rho^* u_3^*, e^*)$, and superscript "*" represents dimensional variables. The Cartesian coordinates, (x^*, y^*, z^*), are represented by (x_1^*, x_2^*, x_3^*) in the tensor notation. In the current simulation of three-dimensional flow over a blunt cone, x^* axis is along the center line of the axisymmetric cone pointing downstream. The origin of the Cartesian coordinate system is located at the center of the spherical nose cone.

For all results presented in this paper, unless specified otherwise, we nondimensionalize the flow velocities by the freestream velocity u_∞^*, length scales by the nose radius r_n^*, density by ρ_∞^*, pressure by p_∞^*, temperature by T_∞^*, time by r_n^*/u_∞^*, etc. The dimensionless flow variables are denoted by the same dimensional notation but without the superscript "*".

A 3-D fifth-order shock-fitting method of Zhong[29] is used to compute the flow field bounded by the bow shock and wall surface. In the discretization of the Navier-Stokes equations, spatial derivatives in the streamwise (s) and wall-normal (y_n) directions are modeled by a fifth-order finite difference schemes. The derivatives in the azimuthal direction (ϕ) are modeled by the Fourier collocation method because of periodicity. The flow variables behind the shock are determined by the Rankine-Hugoniot relations across the shock and a characteristic compatibility equation from behind the shock. The details of the shock fitting formulas and numerical methods can be found in [29].

3 Flow Conditions

The flow conditions for the test case studied in this paper are the same as those in the experiments on air flow over a blunt cone by Stetson et al.[1]. Only the results of one of the cone nose radii are presented in this paper. The specific flow conditions are:

- $M_\infty = 7.99$, $r_n^* = 0.0889m$ $(3.5in)$
- $p_t^* = 4\times10^6$ Pa, $T_t^* = 750$ K
- $\gamma = 1.4$, $\mathrm{Pr} = 0.72$, $R^* = 286.94 Nm/kgK$
- Freestream unit Reynolds number: $\mathrm{Re}_\infty^* = 8.78\times10^6 m^{-1}$
- Blunt cone half angle: $\theta = 7^\circ$, the freestream flow has a zero angle of attack
- Parameters in Sutherland's viscosity law: $T_r^* = 288K$, $T_s^* = 110.33K$, $\mu_r^* = 0.17894\times10^{-4} kg/ms$

where p_t^* and T_t^* are total pressure and total temperature respectively. For the steady base flow without the surface roughness, the body surface is a non-slip and adiabatic wall for the steady base flow solution. The steady base flow is axisymmetric. The simulation is carried out by using 121 grid points between the cone surface and the shock (in the wall-normal direction). The simulation is carried out using many zones in the streamwise direction with 121 grid points per zone. For the simulation with periodic array in the azimuthal direction, a total of 32 points are used to capture 16 Fourier modes in the ϕ direction.

4 Surface Roughness Model

The numerical simulation for the receptivity to the roughness elements are carried out in two steps. First, a steady base flow field without the roughness elements is computed by advancing the flow calculations to convergence with no disturbances imposed in the freestream and no surface roughness. Second, the steady viscous flows are computed again by imposing an isolated or a distributed surface roughness on the cone surface. The steady base flow solution is used as an initial condition for the roughness simulation. In this paper, only a local small roughness element is used so that the roughness effect is linear. Therefore, the roughness elements of different azimuthal mode index n are independent and can be decomposed by a Fourier transform on the perturbation variables. The Fourier transform in the azimuthal direction leads to the perturbation amplitudes and phase angles for each individual azimuthal index n.

In this paper, a 3-D stationary isolated surface roughness element is imposed on the cone surface near the nose region in the following form:

$$h(s,\phi) = \varepsilon h_0 \left(\sum_{n=1}^{N} A_n \cos(2\pi n\phi + \phi_n) \right) f(s) \tag{2}$$

where h_0 is a reference length of the roughness, s is the natural coordinate along the surface curve length measured from the stagnation point, ϕ is the azimuthal angle on the surface, ε is the nondimensional roughness magnitude, n is the azimuthal index. The roughness element consists of a total of $N = 14$ independent modes, which can be separated by a Fourier transorm in ϕ. The mode with an index n is equivalent to an array of n isolated roughness elements in the azimuthal direction. In Eq.(2), A_n and ϕ_n set the relative amplitude and phase angle of the roughness element of index n. Since the roughness effects are linear in the current case, these two values are set to $A_n = 1$ and $\phi_n = 0$ for all n $(n = 1, 2, \cdots, N)$ in this paper.

As stated earlier in this paper, the origin of the Cartesian coordinate system, $(x,\ y,\ z)$, is located at the center of the nose of the spherical cone, where the x coordinate points from left to the right along the center line of the axisymmetric cone. In addition to x, a natural coordinate s is also used in this paper to measure the dimensionless curve length of a surface location starting from the stagnation point. The nondimensional s and x, which are normalized by the nose radius r_n, are related to each other by the following relation:

$$x = \begin{cases} -\cos(s) & (s \le \pi/2 - \theta) \\ (s + \theta - \pi/2)\cos\theta - \sin\theta & (s > \pi/2 - \theta) \end{cases} \tag{3}$$

where θ is the half angle of the cone. In the current test case, $\theta = 7^\circ$.

The shape of the roughness element in the streamwise direction is determined by the shape function $f(s)$ in Eq. (2). In this paper, only an array of isolated roughness elements is considered. In this case, the shape function of the roughness along the streamwise direction is given by a Gaussian distribution as follows:

$$f(s) = \begin{cases} \dfrac{e^{-\alpha[(s-s_0)/L]^2} - e^{-\alpha/4}}{1 - e^{-\alpha/4}} & \left((s_0 - L/2) \le s \le (s_0 + L/2)\right) \\ 0 & \text{otherwise} \end{cases} \tag{4}$$

where s_0 is the location of the center of the roughness hump, L is the length of the element, and α is a non-dimensional parameter controlling the width of the hump.

So far, we have computed one case of the receptivity of the hypersonic flow to a local roughness hump with 14 independent indices n ($N = 14$ in Eq. (2)). The specific parameters for the roughness hump are:

- $L = 2,\ s_0 = 2,\ h_0 = 1,\ \alpha = 0.25,$
- Nondimensional roughness amplitude: $\varepsilon = 10^{-5}$ for a small roughness elements,
- The element consists of a total of 14 azimuthal index: $n = 1, \cdots, 14$.

Since only a small surface roughness element is considered in this paper, linearized boundary conditions are used to model the surface roughness on the cone surface. Specifically, the velocities are set to zero at the wall for the

steady base flow without the roughness. For subsequent simulation of steady flow with surface roughness, a velocity component at the bottom grid line $(j=1)$ on the cone surface is:

$$u_w = -\left(\frac{\partial \bar{u}}{\partial y_n}\right)_w h \tag{5}$$

where $\left(\partial \bar{u}/\partial y_n\right)_w$ is the wall-normal gradient of the steady base flow velocity at the wall, and h is the local wall-normal height of the roughness element. For the perturbed temperature with surface roughness, the temperature is isothermal to the steady flow wall temperature. Hence the temperature at $(j=1)$ with the surface roughness is:

$$T_w = \bar{T} - \left(\frac{\partial \bar{T}}{\partial y_n}\right)_w h \tag{6}$$

These boundary conditions are valid for cases of small surface roughness only. For finite roughness elements, the linearization leading to Eqs. (5) and (6) is not valid. The nonlinear effects of finite surface roughness elements on the receptivity are not considered in this paper.

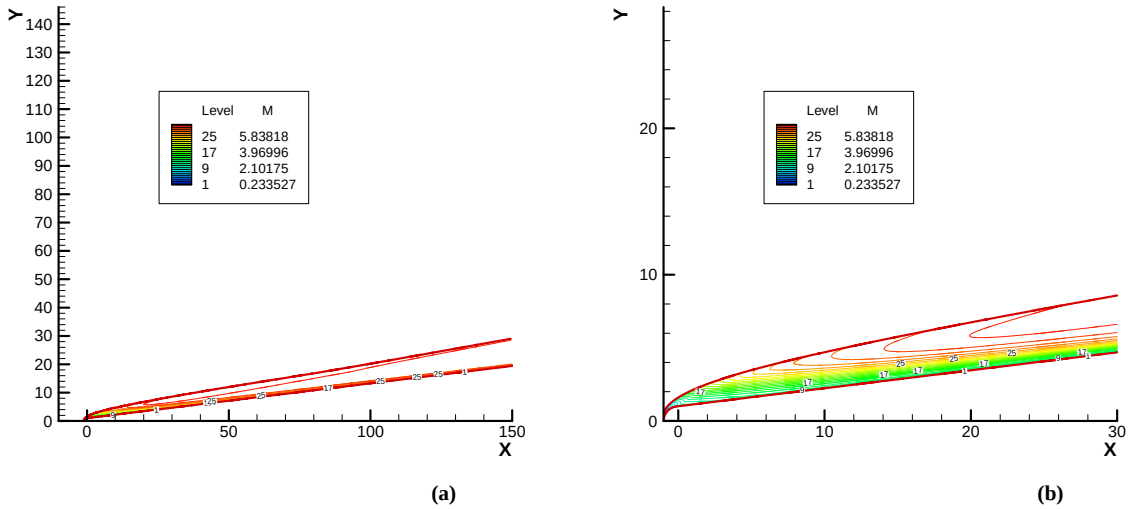

Figure 1. *Mach number contours for steady Mach 7.99 flow over a* 7° *half-angle blunt cone without the roughness where (b) is the same contours enlarged in the local region near the nose.*

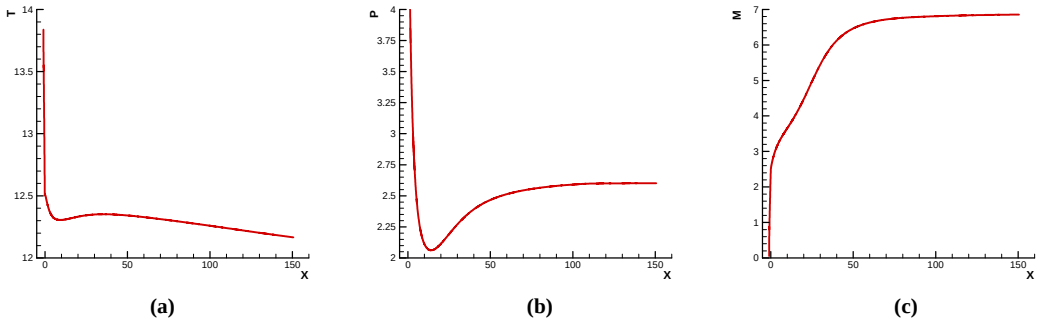

Figure 2. *Profiles of surface temperatures (a), surface pressures (b), and Mach numbers (c) immediately behind the bow shock for the steady base flow without the roughness.*

5 Steady Base Flow Solution without Roughness

The steady base flow solution is obtained first by computing the flow without surface roughness. In [15, 16], the steady base flow solutions of several cases of smaller nose radii were compared with those of Esfahanian and Herbert[17] and the experimental results of Stetson et al. The effects of the nose radius on the steady base flow solutions were also compared. In this paper, we will mainly present the steady base flow solution for the current case of $r_n^* = 88.9mm$.

Figure 1 shows the Mach number contours for steady base flow solution without the surface roughness. The bow shock is obtained as the outer computational boundary of the contours. The figure shows strong effects of the entropy layer near the nose region in Fig. 1(b) for the current case of large nose radius. The profiles of surface temperatures, surface pressures, and Mach numbers immediately behind the bow shock for the steady base flow without the roughness are shown in Fig. 2. These profiles are typical of hypersonic flow over a blunt straight cone with a spherical nose. The maximum wall pressure is reached at the stagnation point. The surface pressure drops sharply as flow expands around the nose region. Because of the discontinuity in surface curvatures at the junction of the spherical nose and straight cone afterward, the flow experiences an over-expansion at the junction and goes through a recompression along the cone surface afterward. As a result, there is adverse pressure gradient along the surface locations after the junction. Further downstream, the surface pressure approaches a constant value. This figure also shows that the nose radius also affects the wall temperature distribution. The maximum steady adiabatic wall temperature is reached at the stagnation point. The temperature drops gradually as s increases along the surface. The distributions of Mach number at locations immediately behind the bow shock are also shown in Fig. 2 (c). The flow is subsonic in the stagnation region. The Mach number increases to a constant value as s increases.

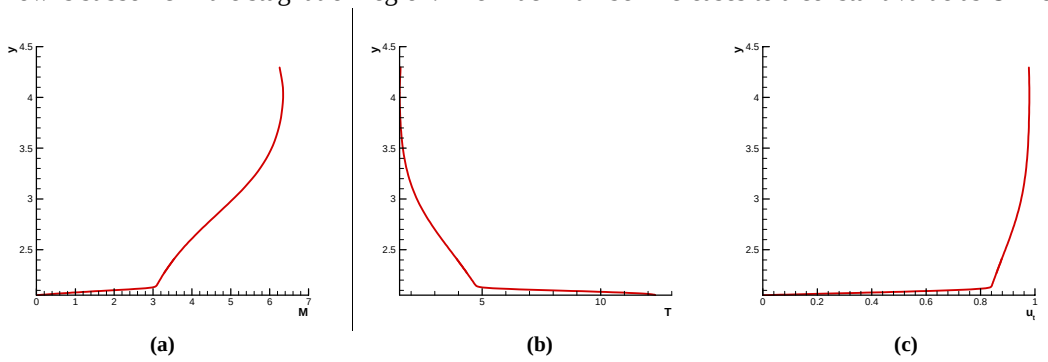

Figure 3. *Profiles of Mach numbers (a), temperatures (b), and tangential velocities (c) along a wall-normal grid line which is originated from a point located at* $x = 8.51$ *on the cone surface.*

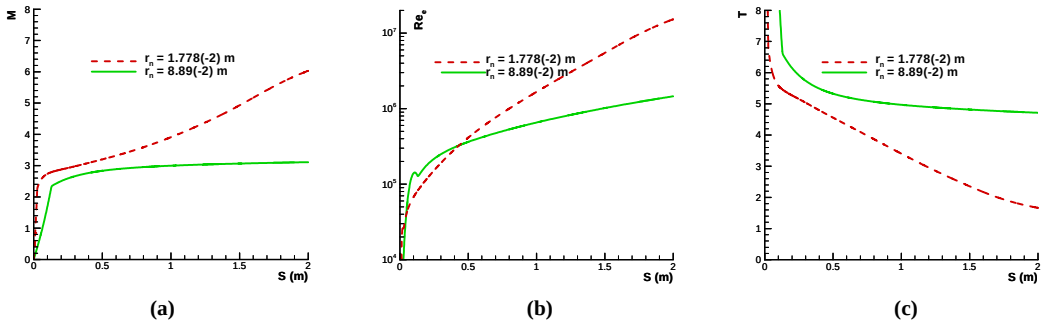

Figure 4*. Comparisons of profiles of Mach numbers (a), local Reynolds numbers (b), and temperatures (c) at the edge of the boundary layer for steady based flow with two cases of different nose radii.*

For this particular flow, the boundary layer is relatively thin compared to the stand-off distance between the bow shock and the cone surface as shown in Fig. 3, which shows the distributions of Mach numbers, temperatures, and tangential velocities along a wall-normal grid line which is originated from a point located at $x = 8.51$ on the cone

surface. The figure shows that the flow conditions at the edge of the boundary layer are very different from those immediate behind the bow shock. The variation of flow variables between the edge of the boundary layer and the bow shock is caused by the entropy layer behind the curved shock.

The main effect of the entropy layer is the reduction of local Reynolds numbers in the mean flow. Figure 4 compares the profiles of Mach numbers, local Reynolds numbers, and temperatures at the edge of the boundary layer for steady based flow with two cases of different nose radii. The dimensional s^* is used in the plots in order to compare two cases of different nose radii. As r_n^* increases, the effect of entropy layer is stronger as shown by the reduction of edge Mach numbers. For the current case of $r_n^* = 88.9mm$, the edge Mach number is around 2.5 in the region near the nose, while the case of $r_n^* = 17.78mm$ has much higher edge Much numbers. Meanwhile the edge temperatures are much higher for the current case. As a result, the local Reynolds numbers along the edge of the boundary layer are much lower for the current case of larger nose radius. The only exception is the small region immediate behind the spherical nose, where the local Reynolds number of the current case is larger. Therefore, the increase of the nose radii results in larger local Reynolds number in the nose region, but smaller Reynolds numbers further downstream.

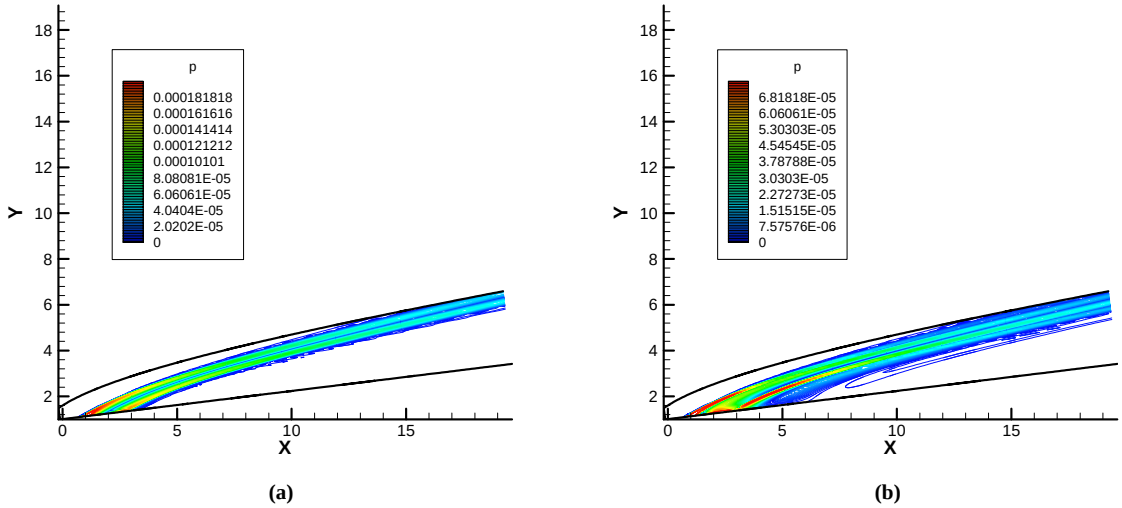

Figure 5. *Magnitude contours of the pressure perturbations for steady flow with local surface roughness for two of the 14 azimuthal modes: (a)* $n = 1$, *(b)* $n = 8$.

6 Receptivity to Azimuthal Array of Isolated Surface Roughness Elements

Having obtained the steady base flow solutions, the receptivity to surface roughness for the same flow is studied by numerical simulation. The surface roughness is imposed in the straight cone region near the spherical nose ($s_0 = 2$ in Eq. (4)). The width of the roughness element in the streamwise direction is two times as long as r_n. There are a total of 14 ($n = 1, \cdots, 14$) independent azimuthal modes in the simulation. The magnitudes for each mode can be separately obtained by a Fourier transform.

Figure 5 shows the magnitude contours of the pressure perturbations for steady flow with local surface roughness for two of the 14 azimuthal modes. The roughness is confined in the region before $x = 3.5$ only. The figure shows the Mach waves generated by the roughness. The roughness is expected to generate streamwise vortices in the boundary layer. The generation of streamwise vortices is related to the variation of the streamwise velocity because of the "lift-up" effect of the vortices. Figures 6 and 7 show the magnitude contours of u

perturbations for steady flow with local surface roughness for two of the 14 azimuthal modes. The roughness elements induce velocity perturbations in the boundary layer behind the roughness. For the case of $n=1$, the velocity perturbations increase as the gas flows downstream. The trend for the case of $n=8$ is opposite where the velocity perturbations decreases along the streamwise direction.

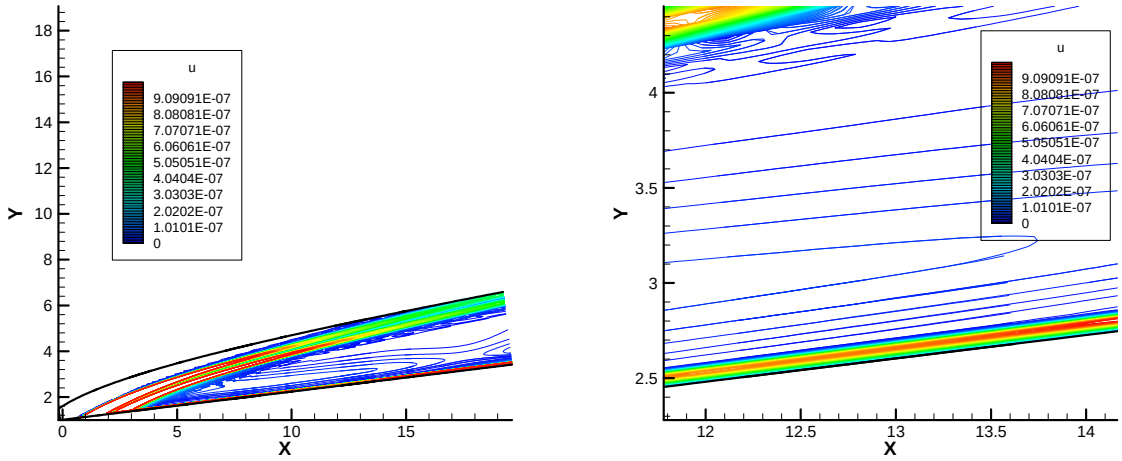

***Figure 6**. Magnitude contours of the horizontal velocity perturbations for steady flow with local surface roughness for $n=1$, where (b) is an enlarged figure of a local region in the boundary layer.*

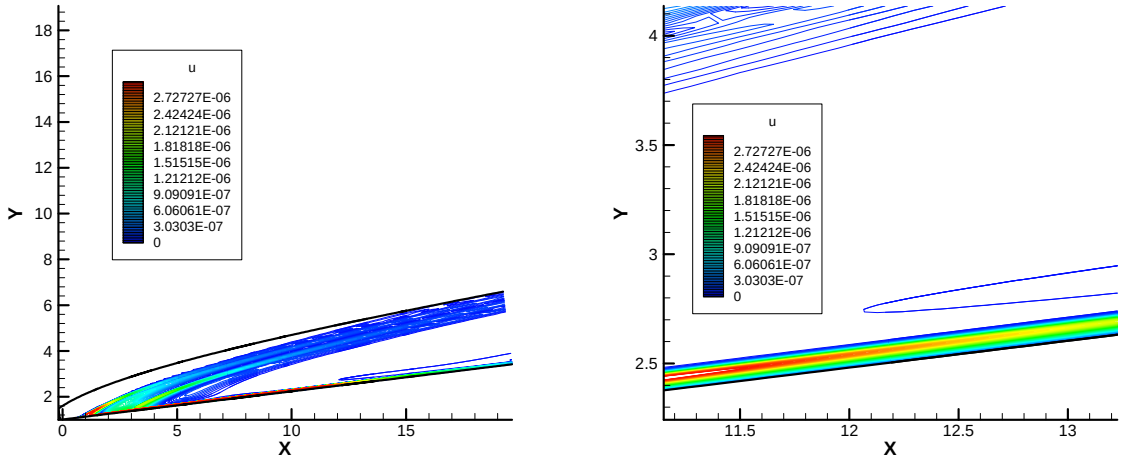

***Figure 7**. Magnitude contours of the horizontal velocity perturbations for steady flow with local surface roughness for $n=8$, where (b) is an enlarged figure of a local region in the boundary layer.*

Figure 8 shows the distribution of u perturbation magnitudes for all 14 modes along a streamwise grid line located near the edge of the boundary layer. The perturbations rise rapidly for flow over the roughness. Downstream of the roughness, the perturbations drop initially for all n. On the other hand, the perturbations for $n=1$ start to increase after the initial drop, while the perturbations for other modes decrease. No obvious strong transient growth can be observed in the current simulation within the limited length of the flow field behind the roughness element. It will be interesting to carry out the simulation to longer computational zone so that the development of the perturbations further downstream can be captured by the simulation. Work in this direction is currently under way.

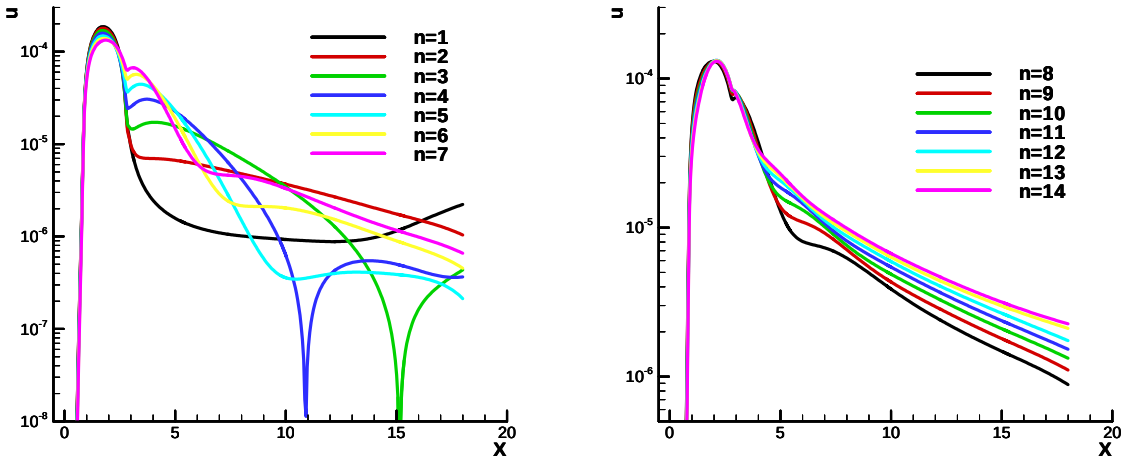

(a) **(b)**

Figure 8*. Distributions of the magnitudes of horizontal velocity perturbations along a streamwise grid line located near the edge of the boundary layer for the 14 modes: (a)* $n = 1, \cdots, 7$ *, (b)* $n = 8, \cdots, 14$ *.*

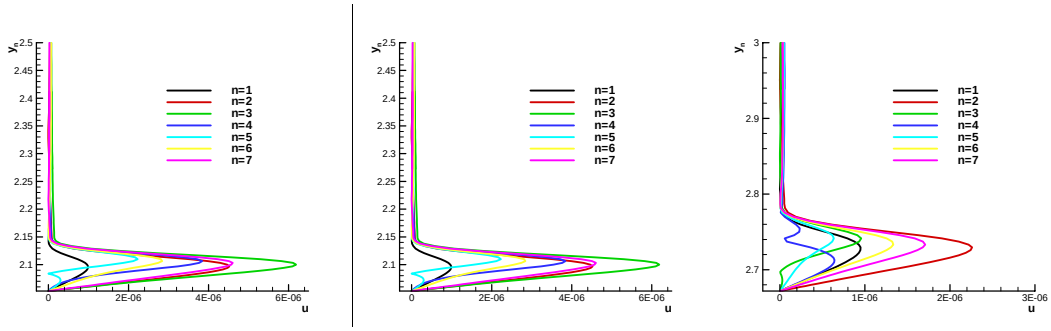

(a) **(b)** **(c)**

Figure 9. *Profiles of the magnitudes of* u *perturbation for 7 modes (*$n = 1, \cdots, 7$*) along three wall-normal grid lines originated at the cone surface: (a)* $x = 2.51$*, (b)* $x = 8.51$*, (c)* $x = 13.6$*.*

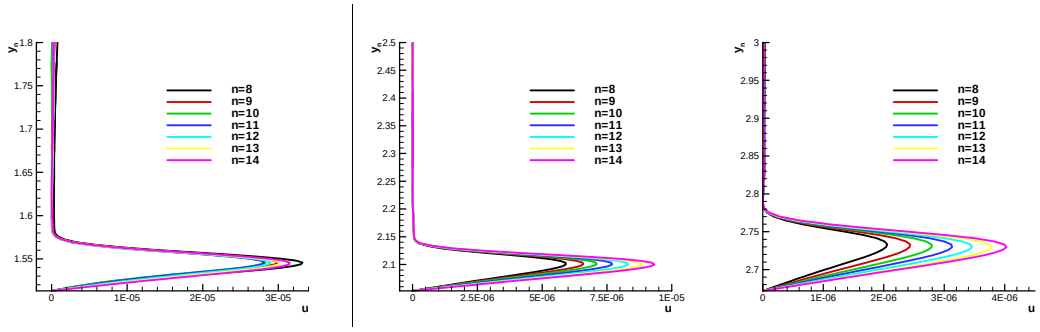

(a) **(b)** **(c)**

Figure 10. *Profiles of the magnitudes of* u *perturbations for 7 modes (*$n = 8, \cdots, 14$*) along three wall-normal grid lines originated at the cone surfac: (a)* $x = 2.51$*, (b)* $x = 8.51$*, (c)* $x = 13.6$*.*

The structure of the wave modes induced by the surface roughness element is examined next. Figures 9 and 10 show the profiles of the magnitudes of horizontal velocity perturbations for all 14 modes along three wall-normal grid lines. Figures 9 (a) and 10 (a) plot the profiles immediately behind the roughness element, while Figs. 9 (c) and 10 (c) are further downstream. The wave profiles are very similar for all n. Most of them have a single peak profile with the peak located near but below the edge of the boundary layer. For example, Fig. 3 shows that the edge of the boundary layer for the (b) is approximately located at $y = 2.13$. Figures 9 (b) and 10 (b) indicate that the peak of the wave profiles for all n are below the edge, with the peaks located near the edge. These two figures also show some interesting double peak features for the perturbation amplitudes for the two azimuthal indices of $n = 4$ and $n = 5$.

Figures 11 and 12 show the cross-sectional view of the contours of temperature and horizontal velocity perturbations for two of the 14 modes. The features for all other modes are similar to those in the figures. For the cases of $n = 1$ and $n = 8$, Fig. 11 shows that the flow decelerates behind the peak of the roughness heights, and accelerates behind the valleys of the roughness element, as a results of the streamwise vortices generated by the surface roughness. On the other hand, the temperatures behind the roughness element increase behind the peak of the roughness heights. The peaks of the temperature perturbations are located at the edge of the boundary layer. All the results indicate the generation of the streamwise vortices by the surface roughness. Further work is needed to conduct extensive simulation on the development of the vortices in much longer computational domains and on the effects of other roughness elements, which include both isolated and distributed roughness.

7 Conclusions

A numerical simulation study has been conducted on the receptivity of Mach 7.99 hypersonic flow over a blunt cone with imbedded azimuthal arrays of isolated surface roughness on the cone surface. The flow conditions are those of Stetson's 1984 wind-tunnel experiments for Mach 7.99 flow over a 7° half-angle blunt cone. The nose radius is 88.9mm. Since only a small surface roughness element is considered in this paper, linearized boundary conditions are used to model the surface roughness on the cone surface. The simulation results show that the roughness element generates streamwise vortices inside the boundary layer. In the computational domain studied in this paper, the induced perturbation mainly decay after the roughness. No strong transient growth appears immediately behind the roughness element. Further studies are needed to study the effects of longer computational domains and the effects of other isolated and distributed roughness elements.

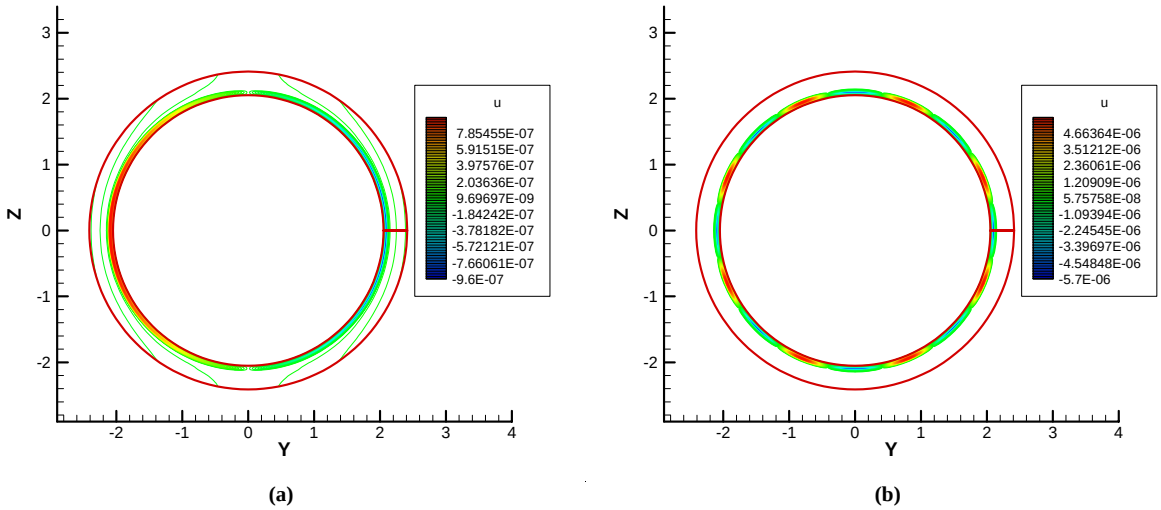

***Figure 11**. Cross-sectional view of the contours of u perturbations for two of the 14 modes: (a) $n = 1$, (b) $n = 8$.*

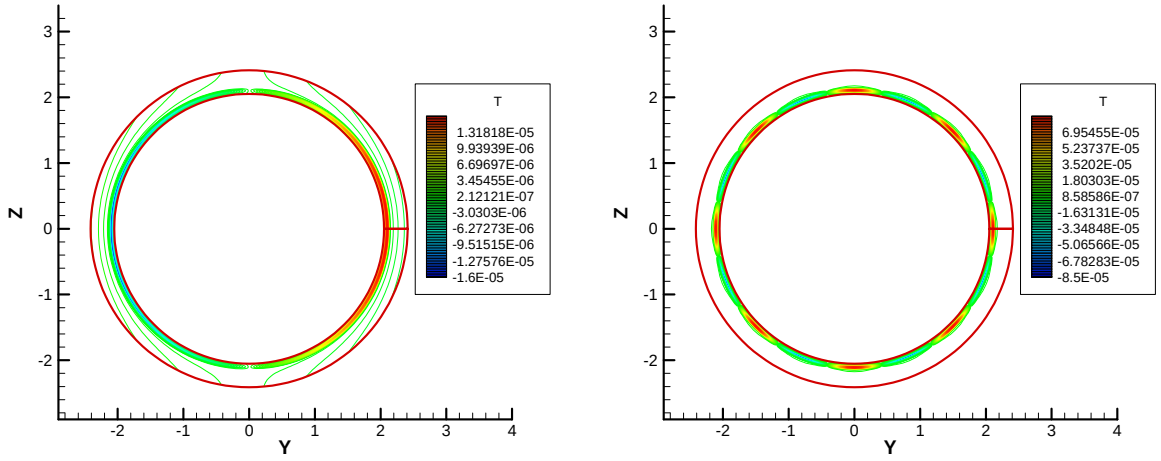

***Figure 12**. Cross-sectional view of the contours of temperature perturbations for two of the 14 modes: (a)* $n = 1$, *(b)* $n = 8$.

Acknowledgments

This work was sponsored by the Air Force Office of Scientific Research, USAF, under AFOSR Grant #FA9550-04-1-0029, monitored by Dr. John Schmisseur. The views and conclusions contained herein are those of the author and should not be interpreted as necessarily representing the official policies or endorsements either expressed or implied, of the Air Force Office of Scientific Research or the U.S. Government.

References

1. **Stetson, K.F., Thompson, E. R., Donaldson, J. C., and Siler, L. G.,** ***Laminar Boundary Layer Stability Experiments on a Cone at Mach 8, Part 2: Blunt Cone.*** **1984. AIAA paper 84-0006.**
2. **Stetson, K.F., and Kimmel, R.,** ***On the Breakdown of a Hypersonic Laminar Boundary Layer.*** **1993. AIAA Paper 93-0896.**
3. **Demetriades, A.,** ***Hypersonic Viscous Flow Over A Slander Cone. Part III: Laminar Instability and Transition.*** **AIAA paper 74-535, 1974.**
4. **Demetriades, A.,** ***Laminar Boundary Layer Stability Measurements at Mach 7 Including Wall Temperature Effects.*** **AFOSR-TR-77-1311, 1977.**
5. **Maslov, A.A., Shiplyuk, A. N., Sidorenko, A., and Arnal, D.,** ***Leading-edge Receptivity of a Hypersonic Boundary Layer on a Flat Plate.*** **Journal of Fluid Mechanics, 2001. 426: p. 73-94.**
6. **Maslov, A.A., Mironov, S. G., Shiplyuuk, A. A., Sidorenko, A. A., Buntin, D. A., and Aniskin, V. M.,** ***Hypersonic Flow Stability Experiments.*** **2002. AIAA 2002-0153.**
7. **Malik, M.R., Spall, R. E., and Chang, C. L.,** ***Effect of Nose Bluntness on Boundary Layer Stability and Transition.*** **1990. AIAA Paper 90-0112.**
8. **Herbert, T., and Esfahanian, V.,** ***Stability of Hypersonic Flow over a Blunt Body.*** **AGARD CP, 1993. 514: p. 28.**
9. **Kufner, E., Dallmann, U., and Stilla, J.,** ***Instability of Hypersonic Flow Past Blunt Cones - Effects of Mean Flow Variations.*** **1993. AIAA paper 93-2983.**
10. **Kufner, E., and Dallmann, U.** ***Entropy and Boundary Layer Instabilityof Hypersonic Cone Flows - Effects of Mean Flow Variations*****. in** ***IUTAM Symposium on Laminar-Turbulent Transition*****. 1994. Sendai/Japan: Springer-Verlag, Berlin.**

11. Rosenboom, I., Hein, S., and Dallmann, U., *Influence of Nose Bluntness on Boundary-Layer Instabilities in Hypersonic Cone Flows* AIAA Paper 99-3591, 1999.
12. Potter, J.L., and Whitfield, J. D. *Boundary-Layer Transition under Hypersonic Conditions*. in *Recent Developments in Boundary Layer Research, Part III*. 1965.
13. Ericsson, L.E., *Effects of Nose Bluntness and Cone Angle on Slender Vehicle Transition.* AIAA Paper 87-1415, 1987.
14. Zhong, X., *Numerical Simulation and Experimental Comparison of Hypersonic Boundary Layer Instability over a Blunt Cone.* AIAA paper 2004-2244, 2004.
15. Zhong, X., and Ma, Y., *Boundary-layer receptivity of Mach 7.99 Flow over a blunt cone to free-stream acoustic waves.* Journal of Fluid Mechanics, 2005. 556: p. 55-103.
16. Zhong, X., *Effect of Nose Bluntness on Hypersonic Boundary Layer Receptivity over a Blunt Cone.* AIAA paper 2005-5022, 2005.
17. Esfahanian, V., *Computation and stability analysis of laminar flow over a blunt cone in hypersonic flow*. 1991, The Ohio State University.
18. Hanifi, A., Schmid, P.J., and Henningson, D.S., *Transient growth in compressible boundary layer flow.* Physics of Fluids, 1996. 8(3): p. 826-837.
19. Reshotko, E., *Transient growth: a factor in bypass transition.* Physics of Fluids, 2001. 13: p. 1067-1075.
20. Reshotko, E., and Tumin, A., *Role of Transient Growth in Roughness-Induced Transition.* AIAA Journal, 2004. 42(4): p. 766-771.
21. Reshotko, E., and Tumin, A., *Spatial theory of optimal disturbances in boundary layers.* Physics of Fluids, 2001. 13(7): p. 2097-2104.
22. Reda, D.C., *Review and Synthesis of Roughness-Dominated Transition Correlations for Reentry Applications.* Journal of Spacecraft and Rockets, 2002. 39(2): p. 161-167.
23. White, E.B., *Transient growth of stationary disturbances in a flat plate boundary layer.* Physics of Fluids, 2002. 14(12): p. 4429-4439.
24. White, E.B., and Rice, J. M., and Ergin, G., *Receptivity of stationary transient disturbances to surface roughness.* Physics of Fluids, 2005. 17(6): p. 064109 1-12.
25. Choudhari, M., and Fischer, P. *Roughness-Induced Transient Growth*. in *35th AIAA Fluid Dyamics Conference*. 2005.
26. Fischer, P., and Choudhari, M. *Numerical Simulation of Roughness-Induced Transient Growth in a Laminar Boundary Layer*. in *34th AIAA Fluid Dynamics Conference*. 2004.
27. Tumin, A., *The Problem of Boundary-Layer Flow Encountering a Three-Dimensional Hump Revisited.* AIAA paper 2004-0101, 2004.
28. Tumin, A. *Receptivity of Compressible Boundary Layers to Three-Dimensional Wall Perturbations*. 2006.
29. Zhong, X., *High-Order Finite-Difference Schemes for Numerical Simulation of Hypersonic Boundary-Layer Transition.* Journal of Computational Physics, 1998. 144: p. 662-709.
30. Zhong, X., *Leading-Edge Receptivity to Free Stream Disturbance Waves for Hypersonic Flow over a Parabola.* Journal of Fluid Mechanics, 2001. 441: p. 315-367.
31. Zhong, X., *Additive Semi-Implicit Runge-Kutta Schemes for Computing High-Speed Nonequilibrium Reactive Flows.* Journal of Computational Physics, 1996. 128: p. 19-31.